



## **KCl acts as a flux to assist the growth of sub-millimeter-scale metallic 2D non-layered molybdenum dioxide**

Downloaded from: <https://research.chalmers.se>, 2025-02-06 10:15 UTC

Citation for the original published paper (version of record):

Deng, L., Zhang, Q., Li, W. et al (2025). KCl acts as a flux to assist the growth of sub-millimeter-scale metallic 2D non-layered molybdenum dioxide. *Rare Metals*, 44(1): 404-416. <http://dx.doi.org/10.1007/s12598-024-02898-0>

N.B. When citing this work, cite the original published paper.



# KCl acts as a flux to assist the growth of sub-millimeter-scale metallic 2D non-layered molybdenum dioxide

Li-Ying Deng, Qing Zhang, Wang-Yang Li, Xiao-Yuan Ye\*, Yi-Fan Zhao, Shen-Zhong Chen, Yu-Lan Wang\*, Xing-Hui Wang\*, Hui-Peng Chen\*, Zhi-Yang Yu\*, Qun Yan\*, Shu-Ying Cheng\*, Tai-Liang Guo\*, Wen-Ping Hu, Feng Ding\*, Jie Sun\*

Received: 16 February 2024 / Revised: 2 April 2024 / Accepted: 2 April 2024 / Published online: 7 August 2024  
© The Author(s) 2024

**Abstract** Two-dimensional (2D) metal oxides (2DMOs), such as MoO<sub>2</sub>, have made impressive strides in recent years, and their applicability in a number of fields such as electronic devices, optoelectronic devices and lasers has been demonstrated. However, 2DMOs present challenges in their synthesis using conventional methods due to their non-van der Waals nature. We report that KCl acts as a flux to prepare large-area 2DMOs with sub-millimeter scale. We systematically investigate the effects of temperature, homogeneous time and cooling rate on the products in the

flux method, demonstrating that in this reaction a saturated homogenous solution is obtained upon the melting of the salt and precursor. Afterward, the cooling rate was adjusted to regulate the thickness of the target crystals, leading to the precipitation of 2D non-layered material from the supersaturated solution; by applying this method, the highly crystalline non-layered 2D MoO<sub>2</sub> flakes with so far the largest lateral size of up to sub-millimeter scale ( $\sim 464 \mu\text{m}$ ) were yielded. Electrical studies have revealed that the 2D MoO<sub>2</sub> features metallic properties, with an excellent sheet resistance as low as  $99 \Omega\text{-square}^{-1}$  at room temperature, and exhibits a property of charge density wave in the measurement of resistivity as a function of temperature.

Li-Ying Deng, Qing Zhang have equally contributed to this work.

**Supplementary Information** The online version contains supplementary material available at <https://doi.org/10.1007/s12598-024-02898-0>.

L.-Y. Deng, H.-P. Chen, Q. Yan, T.-L. Guo, J. Sun\*  
National and Local United Engineering Laboratory of Flat Panel Display Technology, College of Physics and Information Engineering, Fuzhou University, Fuzhou 350100, China  
e-mail: jie.sun@fzu.edu.cn

L.-Y. Deng  
Fujian Key Laboratory of Agricultural Information Sensing Technology, College of Mechanical and Electrical Engineering, Fujian Agriculture and Forestry University, Fuzhou 350002, China

Q. Zhang, W.-P. Hu  
Key Laboratory of Organic Integrated Circuit, Department of Chemistry, School of Science, Ministry of Education and Tianjin Key Laboratory of Molecular Optoelectronic Sciences, Tianjin University, Tianjin 300072, China

Q. Zhang, W.-P. Hu  
Collaborative Innovation Center of Chemical Science and Engineering (Tianjin), Tianjin 300072, China

**Keywords** 2D non-layered materials; Metallic; Metal oxide; Thickness modulation; Flux method

W.-Y. Li, S.-Z. Chen, X.-H. Wang\*, S.-Y. Cheng\*  
College of Physics and Information Engineering, Institute of Micro-Nano Devices and Solar Cells, Fuzhou University, Fuzhou 350108, China  
e-mail: seaphy23@fzu.edu.cn

X.-Y. Ye\*, Y.-L. Wang\*, Z.-Y. Yu\*  
State Key Laboratory of Photocatalysis on Energy and Environment, College of Chemistry, Fuzhou University, Fuzhou 350116, China  
e-mail: yuzyemlab@fzu.edu.cn

Y.-F. Zhao  
Faculty of Materials Science and Engineering/Institute of Technology for Carbon Neutrality, Shenzhen Institute of Advanced Technology, Chinese Academy of Sciences, Shenzhen 518000, China



## 1 Introduction

Two-dimensional (2D) materials of atomic scale exhibit tremendous potential for future semiconductor device applications due to their captivating physical attributes and outstanding optoelectronic capabilities. Based on their microstructure, 2D materials can roughly be divided into two categories: 2D layered and 2D non-layered materials [1–3]. 2D non-layered materials are formed by chemical bonds in three-dimensional (3D) directions, leading to unsaturated dangling bonds on the surface and inducing highly active and energetic surfaces, making them have broad prospects as components of efficient and practical devices [4, 5]. The major categories of 2D non-layered materials include metal dichalcogenides, metals, metal oxides, III–V semiconductors, organic–inorganic perovskites and others [6]. 2D metal oxides (2DMOs) have attracted significant interest in the realms of electronics, electret technology, optoelectronics, lasers, and related fields, primarily due to their unique electrical architectures and diverse surface chemistry [7–13]. MoO<sub>2</sub>, exemplifying the characteristics of 2DMOs, has showcased its utility in magnetism, piezoelectricity, and sensor technologies. For example, Zhang et al. [14] reported that the 2D MoO<sub>2</sub> flakes exhibited a large linear magnetoresistance of up to 455% at 3 K and −9 T and a nonlinear hall effect. Moreover, 2D MoO<sub>2</sub> reveals an unexpected piezoelectric-like response. As reported by Ajayan et al., the 2D MoO<sub>2</sub> exhibited an out-of-plane piezoresponse of 0.56 pm·V<sup>−1</sup>, which is comparable to that of standard 2D piezoelectric materials [15]. In addition to its superior properties resulting from its intrinsic structures, 2D MoO<sub>2</sub> is also

promising to be integrated into heterojunctions to perform some advanced functions. For example, Zou et al. revealed that 2D MoO<sub>2</sub> which is vertically stacked with MoSe<sub>2</sub> as 2D heterostructures exhibited a photoresponsivity of 100.86 mA·W<sup>−1</sup> and a detectivity of 23.4 × 10<sup>9</sup> Jones [16]. However, owing to the inherent non-van der Waals structure of 2D MoO<sub>2</sub>, there has been a lack of effective strategies for the precise cultivation of extensive single crystals, posing challenges to conventional top-down synthesis methods [12]. The lateral size of 2D MoO<sub>2</sub> synthesized via bottom-up methodologies like chemical vapor deposition (CVD) is typically constrained to 10 μm, thereby hindering its subsequent exploration and practical utilization [9, 16–22]. It is essential to develop a versatile growth method for large-area 2D MoO<sub>2</sub> single crystals.

The flux method is considered to be a promising and economical method for the formation of single crystals [23]. The flux method has the benefit of producing crystals with excellent crystallinity and form at a reduced crystallization temperature. Compared with crystals grown from their melt, these crystals typically have fewer defects and are under less strain [24, 25]. In flux growth, the flux is generally a molten salt or oxide that serves as a solvent to dissolve the components of the desired substance [26]. During the reaction, the flux and the precursor are heated to the molten state and the temperature is maintained above the saturation temperature of the solution, after which the target single crystal will precipitate from the supersaturation solution during the cooling down process [27]. The flux method was recorded against various single crystals, from rare earth aluminum borate crystals [28] and insulators [29], to oxide materials [30], etc., but the resultant growth products are typically bulk single crystals, typically millimeters in size on all three dimensions.

While historically, the flux method has been confined to fabricating bulk single crystals utilizing specialized equipment, and there is a lack of explicit reports on its utilization in CVD for synthesizing 2D materials, we do believe it is a feasible approach. The current growth mechanism for 2D materials can be summed up in one of two ways [31–34]: either through a surface-catalyzed process, in which the substrate is essentially not involved in the reaction; or through a precipitation process, in which the target product's constituents are dissolved in the substrate and precipitate out upon cooling. The main distinctions between the two are: (a) The solubility of the target component in the substrate or precursor at the reaction temperature. If the solubility is high, the growth is predominantly precipitation-based. (b) The effect of cooling rate on the thickness of the target product. The cooling rate has a significant impact on thickness in the precipitation process but has little effect on the catalysis process. According to the dissolution-based reaction mechanism of

X.-H. Wang, H.-P. Chen\*, Q. Yan\*, S.-Y. Cheng,  
T.-L. Guo\*, J. Sun  
Fujian Science and Technology Innovation Laboratory for  
Optoelectronic Information of China, Fuzhou 350100, China

Q. Yan  
Rich Sense Electronics Technology Co., Ltd., Quanzhou 362200,  
China

F. Ding  
Center for Multidimensional Carbon Materials, Institute for  
Basic Science (IBS), Ulsan 44919, Korea

F. Ding\*  
Department of Material Science and Engineering, Ulsan  
National Institute of Science and Technology, Ulsan 44919,  
Korea  
e-mail: f.ding@unist.ac.kr

J. Sun  
Department of Microtechnology and Nanoscience, Quantum  
Device Physics Laboratory, Chalmers University of Technology,  
Gothenburg 41296, Sweden

the flux method and its product size can be controlled by the cooling rates [35], we believe that flux growth belongs to the precipitation method.

Considering the ability to lower the melting point of the reactants and the use of salt in the precursor, similarities can be found between the flux method and the “molten-salt-assisted method” (MSAM) frequently reported in the literature for the preparation of large-area 2D materials. Here, we endeavor to illustrate that the MSAM fundamentally aligns with the flux approach rather than representing a catalytic methodology, as the salt typically dissolves the precursor and engages in a reactive process with it. In fact, there are some MSAM reports demonstrating that their target low-dimensional single crystals are precipitated from supersaturated droplets [36–38], in agreement with the flux method we claim. Although the MSAM has been widely employed for the synthesis of various 2D materials, particularly transition-metal chalcogenides [39], there is a notable scarcity of reports pertaining to non-layered 2D materials. This may be ascribed, at least in part, to the lack of understanding of the detailed mechanism, such as how the MSAM regulates the thickness of 2D materials. Indeed, the capability of the flux method to modulate thickness through manipulation of the temperature span and cooling rate underscores its promise in synthesizing non-layered 2D materials such as 2DMOs.

Here, we apply the flux growth strategy in CVD to realize the large-scale preparation of 2D non-layered MoO<sub>2</sub>, elucidating that the essence of reducing the thickness and enlarging the area of the products lies in a supersaturated homogeneous solution and an appropriate cooling rate. In our flux method, the 2D non-layered MoO<sub>2</sub> single crystals precipitated out of the supersaturated solution formed by the precursors and the salt. Through meticulous control of the reaction temperature, homogeneous time and cooling rate, we successfully achieved the largest known non-layered 2DMOs crystals to date [7, 9, 16–21, 40], with thickness effectively regulated by the temperature range and cooling rate. Electrical studies revealed that the obtained 2D MoO<sub>2</sub> crystals featured a metallic nature, with a sheet resistance as low as 99  $\Omega$ -square<sup>-1</sup> at room temperature. Moreover, we observed the occurrence of the charge density wave phenomenon at low temperatures. We thus clarify that the prevailing MSAM is in essence a flux method. Armed with this pivotal comprehension, the experimental conditions can be deliberately optimized toward the flux method. This approach offers an expeditious avenue for the fabrication of large-scale 2D MoO<sub>2</sub> and harbors potential for expansion to additional 2DMOs or layered materials, thereby enhancing their attributes and accelerating their utilization across various domains.

## 2 Experimental

### 2.1 Synthesis of MoO<sub>2</sub> flakes

The flux-grown MoO<sub>2</sub> flakes were grown via CVD, 20 mg MoO<sub>3</sub> (Shanghai Aladdin Bio-Chem Technology Co., LTD, 99.9%), and 5 mg KCl powder was positioned in an alumina crucible placed in the middle of a 1-inch-diameter quartz tube furnace. The SiO<sub>2</sub>/Si substrate (cleaned with acetone, alcohol and deionized water) was set on the same crucible and kept directly above the mixture powder. During the first ten min, the quartz tube was cleaned with 300 ml·min<sup>-1</sup> of highly pure Ar carrier gas. To eliminate pollutants (moisture or organic) that may have been present in the system, the furnace was kept at 150 °C for 10 min. Following this, the temperature is raised to 900 °C in fifty minutes with 30 ml·min<sup>-1</sup> of Ar flow. The temperature is maintained for 30 min and then cooled to room temperature. The flux-free MoO<sub>2</sub> flakes were grown via CVD, too. The experimental conditions were the same as for the flux method, except that no flux (KCl) was added.

### 2.2 Characterization of MoO<sub>2</sub> flakes

Atomic force microscope (AFM, NT-MDTNEXT), optical microscope (OM, OLYMPUS BX51M), Raman spectroscopy (Invia Reflex with an excitation wavelength of 532 nm laser), scanning electron microscope (SEM, Helios G4 CX), X-ray diffraction (XRD, Rigaku Ultima IV), thermogravimetric study (TG, STA449C/6/G), X-ray photoelectron spectroscopy (XPS, Thermo Scientific K-Alpha), transmission electron microscopy (TEM, JEM2800 and Talos F200S), and aberration-corrected scanning transmission electron microscopy (AC-STEM, Themis Z) were used. For TEM sample, the flakes were transferred to the Cu grid via the polymethyl methacrylate (PMMA)-assisted transfer method. Spin-coating PMMA (950 A4) onto MoO<sub>2</sub> of SiO<sub>2</sub>/Si (1500 r·min<sup>-1</sup>, 1 min, twice) was followed by annealing at 150 °C for 5 min. A solid piece of polydimethylsiloxane (PDMS) then adhered to MoO<sub>2</sub> covered by the PMMA and cured at 80 °C for 1 min. After a day of immersion in deionized water (DI water) which caused the spontaneous penetration of the water into the interface between PDMS/PMMA/MoO<sub>2</sub> and SiO<sub>2</sub>/Si, the PDMS/PMMA/MoO<sub>2</sub> was then carefully delaminated from SiO<sub>2</sub>/Si with the assistance of tweezers. The acquired film was then fished by a Cu grid. Lastly, the PDMS was separated from the PMMA after heating at 150 °C for 5 min, and then the PMMA was removed after being immersed in acetone for 20 min. Before further processing, the transferred MoO<sub>2</sub> was washed two times with DI water and ethanol and, finally, dried in N<sub>2</sub> gas.



Schematic illustrations of the crystal structures were drawn using the program VESTA [41].

### 2.3 Device fabrication and measurements

The 150 nm-thick gold electrodes were transferred onto the MoO<sub>2</sub> flakes by probes to construct the two-terminal devices. Using a probe station accompanied by a semiconductor property analyzer, the electrical performance of the MoO<sub>2</sub> devices was measured in ambient conditions with a standard setting (Model: 4200, Keithley, USA). For the temperature-dependent measurement of resistivity, the MoO<sub>2</sub> devices were firstly bonded in open air followed by assembling on a cryostat with a 1-Pa low-pressure chamber. The temperature of the cryostat can be adjusted between 77 and 267 K.

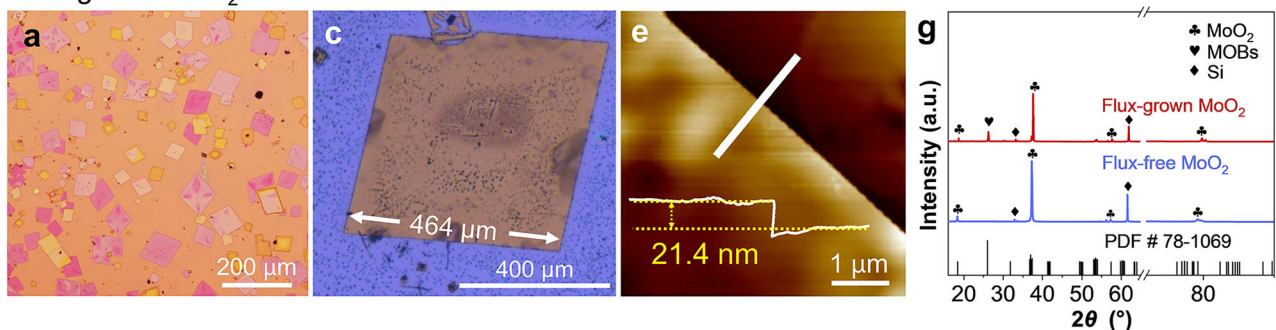
## 3 Results and discussion

### 3.1 Characterizations of MoO<sub>2</sub>

MoO<sub>2</sub> prepared with and without the flux method is denoted as flux-grown and flux-free MoO<sub>2</sub>. The diagram of two CVD installations is shown in Fig. S1a, b. Figure 1 illustrates the differences between the two kinds of MoO<sub>2</sub>. In sharp contrast to the dense nanometer-level cubes of the

flux-free MoO<sub>2</sub> (OM image of Figs. 1b, S1c, d), the lateral length of the flux-grown MoO<sub>2</sub> is tens or even hundreds of microns (Fig. 1a). As shown in OM image in Fig. 1c, the lateral size of the flux-grown sample is as large as 464  $\mu\text{m}$ , which to our knowledge is largest in size of non-layered 2DMO single crystals ever prepared by CVD, and much larger than the numerous studied WO<sub>2</sub> and K-MnO<sub>2</sub>, and so on (Table S1) [7]. The typical lateral size of flux-free MoO<sub>2</sub> is only 257 nm as shown in SEM image in Fig. 1d. It demonstrates that the flux method has the powerful ability to obtain large-area materials in comparison to the conventional CVD method. In addition, it also shows the ability to decrease the dimension of the products from 3 to 2D. As shown in Fig. 1e, f, AFM images show single-crystal flakes with thicknesses of 21.4 nm for flux-grown MoO<sub>2</sub> and 192.5 nm for flux-free MoO<sub>2</sub> (Fig. S2). To illustrate the differences between our flux-free MoO<sub>2</sub> samples and the flux-grown samples more intuitively, we tallied the lateral size and thickness of the products as shown in Fig. S3. The size of the flux-grown MoO<sub>2</sub> is in the range of 20–460  $\mu\text{m}$  with an average lateral size of around 95.7  $\mu\text{m}$  (Fig. S3a), and the thickness distribution reveals the average thickness of flux-grown MoO<sub>2</sub> is 15.8 nm with a range of 5–30 nm (Fig. S3b), and the thinnest 2D MoO<sub>2</sub> we obtained is 6.5 nm, as shown in Fig. S3c. However, for the flux-free MoO<sub>2</sub>, the average lateral size is only about 0.32  $\mu\text{m}$  in the range of 0–1.2  $\mu\text{m}$  (Fig. S3d), while for the

#### Flux-grown MoO<sub>2</sub>:



#### Flux-free MoO<sub>2</sub>:

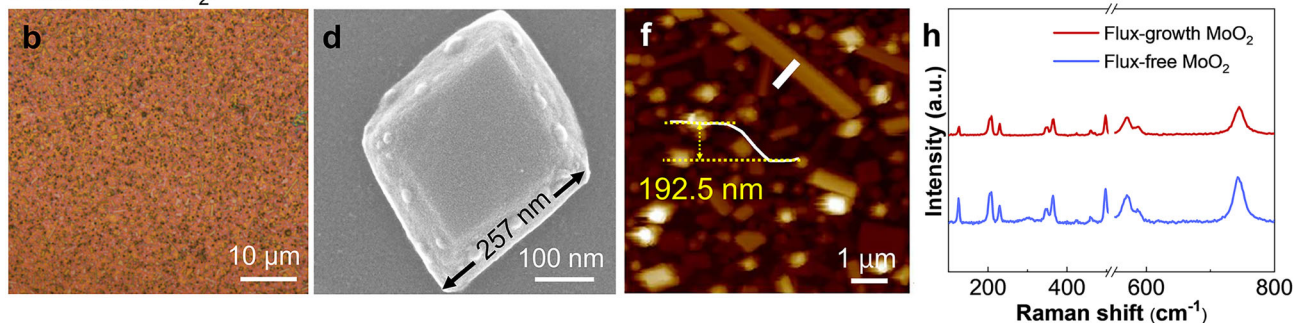


**Fig. 1** Characterizations of MoO<sub>2</sub> flakes with and without flux method: typical OM images of **a** flux-grown MoO<sub>2</sub> flakes and **b** flux-free MoO<sub>2</sub> flakes; typical SEM images of **c** flux-grown MoO<sub>2</sub> flake and **d** flux-free MoO<sub>2</sub> flake; AFM images of **e** single flux-grown MoO<sub>2</sub> flake and **f** flux-free MoO<sub>2</sub> flake; **g** XRD patterns and **h** Raman spectra of flux-grown and flux-free MoO<sub>2</sub> flakes

flux-free MoO<sub>2</sub> an average thickness of  $\sim 110.5$  nm is in the range of 0–300 nm (Fig. S3). XRD result in Fig. 1g demonstrates that the flux-grown MoO<sub>2</sub> and the flux-free MoO<sub>2</sub> flakes have identical crystal structures, which match well with the MoO<sub>2</sub> monoclinic symmetry crystal structure. Thus, the flux method is promising to produce high-quality 2D non-layered single crystals. In Raman spectra (Fig. 1h), we observed the same MoO<sub>2</sub> peaks at 125, 206, 229, 345, 364, 460, 497, 569, 587 and 744 cm<sup>-1</sup> in both two samples [42]. The bands at 587 and 744 cm<sup>-1</sup> are characteristics of MoO<sub>2</sub> and can be attributed to the Mo–O bond stretching

vibrations [43]. From the comparison, it is found that the use of the flux method facilitates the successful fabrication of thinner and larger MoO<sub>2</sub> flakes which is more suitable for device applications.

Following the initial assessment of the quality of the samples, we proceeded with the characterization of its atomic structure to gain a comprehensive understanding of its internal arrangement, aiming to provide insights into the underlying growth mechanisms. The crystalline and surface structure of the flux-grown MoO<sub>2</sub> flakes was studied using AC-STEM. Figure 2a shows a typical rhombic MoO<sub>2</sub>

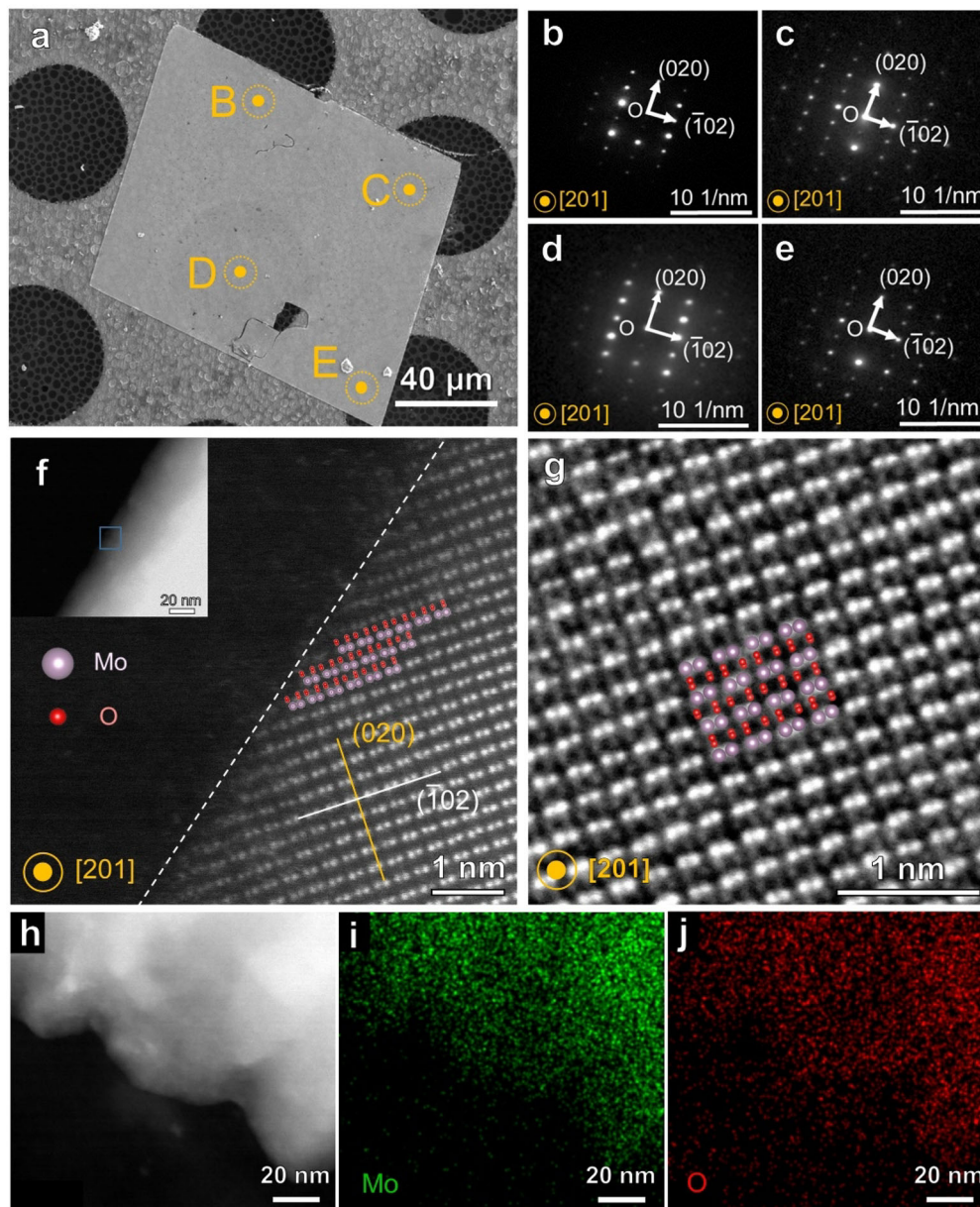


**Fig. 2** STEM images of transferred flux-grown MoO<sub>2</sub> flakes: **a** SEM image of transferred MoO<sub>2</sub> domain on a Cu grid; **b–e** corresponding SAED patterns extracted from different regions as outlined by yellow dots B, C, D and E in **a**; **f, g** AC-IDPC and HAADF images of MoO<sub>2</sub> flake viewed along [201] zone axis and (inset) low-magnification HAADF image; **h** low-magnified HAADF image on edge of flux-grown MoO<sub>2</sub> flake and **i, j** corresponding EDS maps of Mo and O



domain with an edge length of 114  $\mu\text{m}$ . Selected area electron diffraction (SAED) patterns (Fig. 2b–e) extracted from its different areas (yellow dots in Fig. 2a) exhibit well-resolved 2D lattices, where the spacings of 0.28 and 0.24 nm correspond to the (102) and (020) planes of MoO<sub>3</sub>, respectively. The integrated differential phase contrast (iDPC) technique, which offers the advantages of simultaneous imaging of heavy and light atoms [44], was employed to image Mo and O columns. As seen in Fig. 2f, g, the iDPC combined with the high-angle annular dark-field STEM (HAADF-STEM) clearly resolves the periodic arrangement of Mo and O columns, without any discernible vacancy (Fig. S4). Finally, EDS maps confirm that Mo and O elements are homogeneously distributed within the MoO<sub>2</sub> flake, as shown in Fig. 2h–j.

The dominantly exposed surface of these highly crystalline flakes, also defined as their basal habit planes, is assigned to the (100) plane, after considering the crystallography of MoO<sub>2</sub> (see the shaded planes from two orthogonal directions in Fig. 3a, b). The surface energies of 15 possible reconstructed (001), (010) and (100) surfaces of MoO<sub>2</sub> crystal as a function of oxygen chemical potential are tested by density functional theory (DFT) calculations

in Fig. 3c. It is evident that the MoO<sub>2</sub> (100)-1 surface terminated by excess O atoms (Fig. 3c) is the most stable one over a large oxygen chemical potential range, from O-poor limit to O-rich environment (see Calculation Methods in Supplementary Information). This agrees well with the fact that MoO<sub>2</sub> platelets prefer to expose (100) basal facets; therefore, we depicted the schematic illustration of MoO<sub>2</sub> crystal growth in Fig. 3d, vividly depicting the dynamic formation process of MoO<sub>2</sub> crystal with (100) facets as preferential surface.

### 3.2 Mechanism of flux-grown 2D MoO<sub>2</sub>

What makes the flux method successfully obtain the 2D MoO<sub>2</sub>? Here, we propose the reaction mechanism. First, the reaction temperature needs to be high enough to completely dissolve all the constituent parts and form a saturated solution, as only then can the crystals precipitate out from the solution as the supersaturation point is reached when the temperature is lowered [24]. Second, it is essential to keep the reaction temperature a sufficient time until a homogeneous solution is obtained [26]. The appropriate cooling rate is the third consideration. The flux

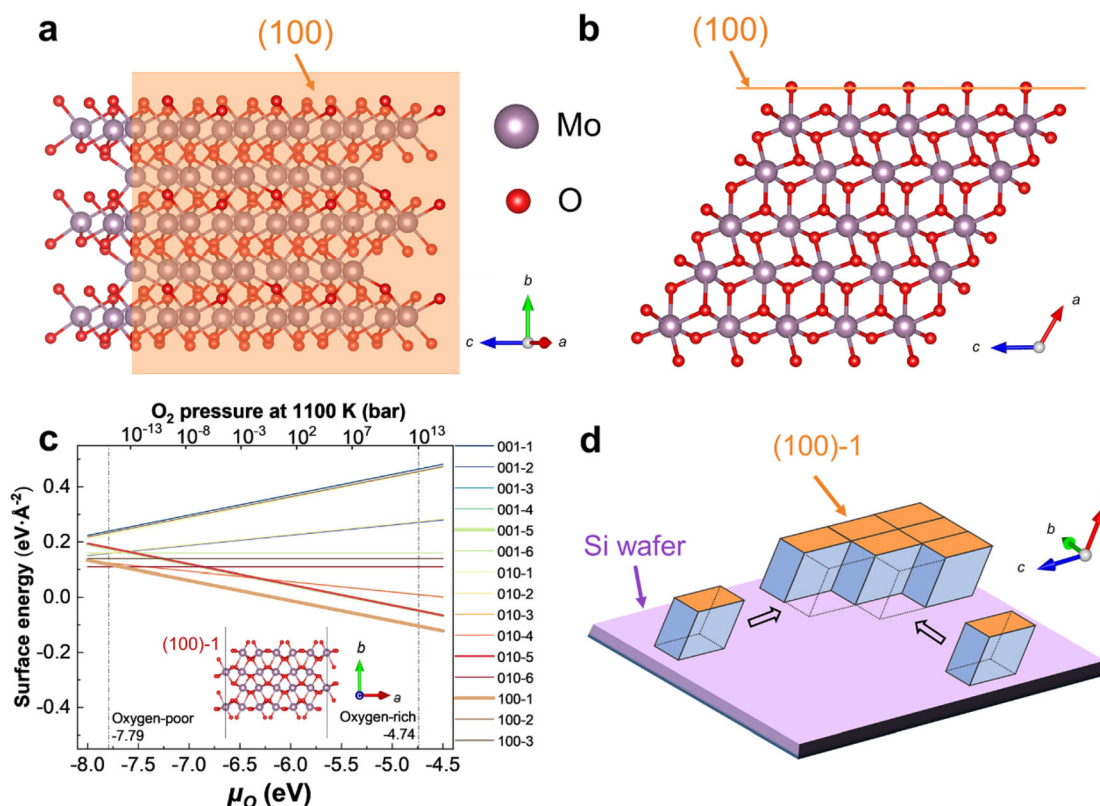


**Fig. 3** Atomic structure of flux-grown MoO<sub>2</sub> flakes: **a** crystal structure of MoO<sub>2</sub> projected along [201] direction, with the electron beam oriented perpendicular to surfaces of platelet, as illustrated by the shaded plane; **b** shade plane rotated 90° around beam direction and (100) plane projected as a line in right panel; **c** surface energies of 15 possible reconstructed (001), (010) and (100) surfaces of MoO<sub>2</sub> crystal as a function of oxygen chemical potential and (inset) illustration of MoO<sub>2</sub> (100)-1 surface; **d** schematic illustration of MoO<sub>2</sub> crystal growth

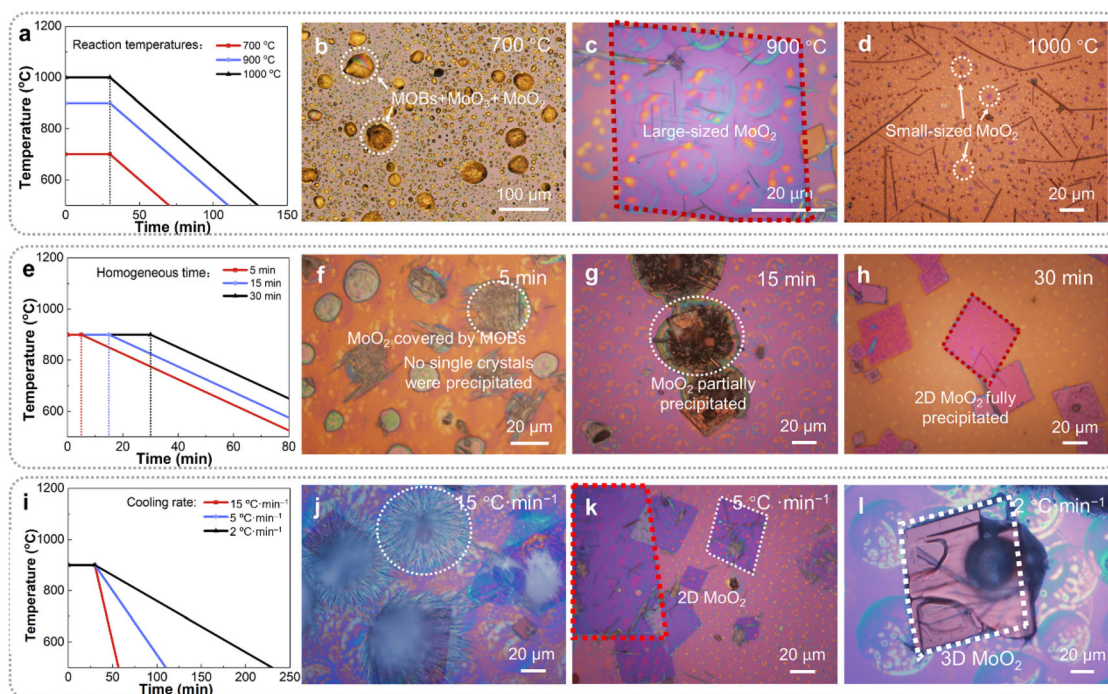


**Fig. 4** Influence of key parameters on preparation of 2D MoO<sub>2</sub> by flux method: **a** time–temperature curves of experiments investigating effect of reaction temperature on products; typical OM images of samples maintained at **b** 700, **c** 900 and **d** 1000 °C for 30 min before cooling to room temperature at 5 °C·min<sup>−1</sup>; **e** time–temperature curves of experiments investigating effect of homogeneous time on products; typical OM images of samples held at 900 °C for **f** 5, **g** 15 and **h** 30 min and then cooled to room temperature at 5 °C·min<sup>−1</sup>; **i** time–temperature curves of experiments investigating effect of cooling rate on products; typical OM images of samples after holding at 900 °C for 30 min and then cooling to room temperature at **j** 15, **k** 5 and **l** 2 °C·min<sup>−1</sup>

method is generally applicable to bulk single crystals. However, the thickness of the target crystal and the cooling rate are highly related, and the key to growing 2D crystals is to control their cooling rate [45]. The pivotal factors influencing the reaction encompass temperature, homogeneous time and cooling rate. We selected the readily available KCl to dissolve the precursor, MoO<sub>3</sub> [16, 17, 20, 46, 47].

We first conducted experiments to illustrate the effect of temperature. Thermogravimetric analysis suggests that KCl and MoO<sub>3</sub> start to react at 510 °C (Fig. S5). The temperature range in our experiment was thus set from 700 to 1000 °C. Results were recorded at each temperature (maintained for 30 min before cooling to room temperature at 5 °C·min<sup>−1</sup>). The corresponding time–temperature curve is shown in Fig. 4a. The typical OM image for the experiment is depicted in Fig. 4b–d, which contains distributed circular particles when cooled from a starting temperature of 700 °C (Fig. 4b), indicating a condensation process. The particles are composed of potassium molybdenum oxide bronzes (MOBs), i.e., K<sub>2</sub>Mo<sub>3</sub>O<sub>10</sub>, K<sub>2</sub>Mo<sub>2</sub>O<sub>7</sub>, K<sub>2</sub>MoO<sub>4</sub> and MoO<sub>3</sub> based on SEM, Raman and energy dispersive X-ray spectrometry (EDS) analyses in Fig. S6a–c [48–51]. Although no clear MoO<sub>2</sub> grains can be found and

confirmed, and neither does MoO<sub>2</sub> exhibit a 2D morphology, several Raman peaks of MoO<sub>2</sub> are present at 126, 229 and 367 cm<sup>−1</sup> [52]. We speculate that the Raman signal of MoO<sub>2</sub> comes from its spontaneous nucleation during the cooling process [26, 53]. A control experiment without salt reveals that there are only a few MoO<sub>3</sub> sheets on the substrate (Fig. S6d–f). Next, it was discovered that 2D MoO<sub>2</sub> flakes were obtained at 900 °C as shown in Figs. 4c, S7. Moreover, different from the typical growth substrate of 2D materials, many bubbles are exhibited on the surface beneath every MoO<sub>2</sub> flake (Fig. S8). These are attributed to the reaction of KCl and MoO<sub>3</sub> to produce a mixed solution containing MOBs. Most MOBs melted at 900 °C, (K<sub>2</sub>Mo<sub>2</sub>O<sub>7</sub> melted at ~ 560 °C, K<sub>2</sub>MoO<sub>4</sub> at ~ 900 °C and MoO<sub>3</sub> at ~ 795 °C) [36, 48]. For the 1000 °C-sample, only a few MoO<sub>2</sub> flakes with a size of just a few microns could be found on the surface, as displayed in Fig. 4d. Consequently, we can conclude that 900 °C is the most suitable temperature for preparing the large-area 2D MoO<sub>2</sub> flakes in our flux growth method.

After determining the holding temperature of 2D MoO<sub>2</sub>, further investigation of the homogenization process of 2D MoO<sub>2</sub> prepared by flux growth is essential to understand the whole growth process. Because flux growth



is achieved by dissolving the precursor with flux to form a saturated solution, after which the target crystals precipitate out of the supersaturated solution during the cooling process, the saturated solution is prepared by holding the composition and flux of the desired crystals at a temperature slightly above the saturation temperature for long enough to form a complete solution, a process known as homogenization [45].

We designed a series of experiments that only altered the holding times at 900 °C to explore the effect of the homogenization process on the resulting products. The corresponding time–temperature curve is shown in Fig. 4e. We present OM images of the products prepared under different conditions, where the reaction times were kept at 900 °C for 5, 15, 30 and 60 min, respectively, followed by cooling to room temperature at 5 °C·min<sup>−1</sup>. After holding at 900 °C for 5 min, the corresponding Raman analysis was conducted as shown in Fig. S9a. The result shows that the particles are made up of K<sub>2</sub>Mo<sub>3</sub>O<sub>10</sub>, K<sub>2</sub>Mo<sub>2</sub>O<sub>7</sub>, K<sub>2</sub>MoO<sub>4</sub>, MoO<sub>3</sub> and MoO<sub>2</sub>, too. As can be surmised, with a holding time of only 5 min, the saturated solution of MoO<sub>2</sub> may not have formed yet and the characteristic peak position of MoO<sub>2</sub> still did not appear, so no single crystals were precipitated (Fig. 4f). After holding for 15 min and dropping to room temperature, as shown in Fig. 4g, some of the MoO<sub>2</sub> had separated from the round particles, indicating that the homogenization process had started, and MoO<sub>2</sub> partially precipitated from the supersaturated solution. Then, after homogenization at this temperature for 30 min, MoO<sub>2</sub> single crystals were formed in Fig. 4h, demonstrating that holding at 900 °C for 30 min permits the homogenization process to be finished and complete 2D MoO<sub>2</sub> single crystals to precipitate. Ultimately, as the homogenization time extends to 60 min, conspicuous circular formations emerge on the substrate, accompanied by a central darkening (Fig. S9b). Notably, the substrate manifests a discernible degree of impairment, devoid of discernible 2D crystals. This occurrence may be attributed to the protracted presence of a corrosive solution containing MOB [54], stemming from an overly prolonged homogenization interval, causing substrate degradation. This deduction underscores the optimal homogenization period of 30 min under our experimental regimen.

It is crucial to continue looking at the cooling rate after obtaining the saturated homogenous solution of 2D MoO<sub>2</sub>. The cooling rate affects the thickness of crystals from flux growth [45]. Therefore, the key to expanding the flux method, which was previously limited to preparing bulk single crystals, to 2D non-layered materials is to control its cooling rate. To illustrate the effect of cooling rate on samples, we designed a series of experiments, varying only the cooling rate of the 900 °C-grown samples. The corresponding time–temperature curve is shown in Fig. 4i.

OM images of thus-prepared products precipitated by different cooling rates of 15, 5 and 2 °C·min<sup>−1</sup> are illustrated in Fig. 4j–l. As shown in Fig. 4j, if the cooling rate is as rapid as 15 °C·min<sup>−1</sup>, MoO<sub>2</sub> is obtained with a large number of MOB atoms. However, the quality of the MoO<sub>2</sub> crystals will be compromised by the rapid cooling rate [24]. When the rate is 5 °C·min<sup>−1</sup>, well-shaped 2D MoO<sub>2</sub> crystals are produced, with only a few MOB atoms present (Fig. 4k). The slow cooling rate of 2 °C·min<sup>−1</sup> yields 3D MoO<sub>2</sub>, as shown in Fig. 4l. Therefore, in the flux method, non-layered 2D MoO<sub>2</sub> with good crystal quality can only be obtained at a suitable cooling rate of around 5 °C·min<sup>−1</sup>.

This precipitation process has been demonstrated by the presence of particulate residues on the surface of the 2D MoO<sub>2</sub> flakes, which were examined by SEM, Raman and EDS. As can be seen in Fig. 5a, several hexagonal-shaped particles are neatly aligned, and EDS and Raman results assist in confirming the presence of K<sub>2</sub>Mo<sub>2</sub>O<sub>7</sub>, K<sub>2</sub>Mo<sub>3</sub>O<sub>10</sub> and K<sub>2</sub>MoO<sub>4</sub> on the surface of the MoO<sub>2</sub> as illustrated in Fig. 5b, c. Moreover, SEM and EDS were randomly conducted around MoO<sub>2</sub> flakes as shown in Fig. S9c–f, it can be distinctly observed that there are particles underneath each MoO<sub>2</sub> flake which are confirmed by EDS result to be most likely potassium MOB. It's worth noting that these residues are all soluble in water and can be removed by using deionized water, as shown in Fig. S10. Based on these findings, it can be assumed that after the homogenization process is complete, the majority of the MOB and MoO<sub>3</sub> are converted to MoO<sub>2</sub>, allowing the MoO<sub>2</sub> to precipitate out during the cooling process, with a small amount of residual MOB being present around the MoO<sub>2</sub> single crystal. Next, the products were collected and analyzed by XPS. Three groups of the fitted curve of Mo 3d (3d<sub>5/2</sub> and 3d<sub>3/2</sub>) are shown in Fig. 5d. The curves at 229.2 and 232.2, 230.9 and 234.2 eV are assigned to the oxidation state of Mo<sup>4+</sup>, which is expected from the stoichiometry of MoO<sub>2</sub> and MoO<sub>x</sub>Cl<sub>y</sub>, while the third group is 232.9 and 235.9 eV, corresponding to Mo<sup>6+</sup>, which together with the signal from K 2p can be explained by the presence of MOB (Fig. 5e). The signals from Cl–Mo bonds in Cl 2p confirm the existence of the MoO<sub>x</sub>Cl<sub>y</sub> (Fig. 5f) [39, 55, 56]. Thus, the existence of MOB and MoO<sub>x</sub>Cl<sub>y</sub> in the preparation process can be confirmed from the experimental results.

Based on the results, a growth model for the flux-grown MoO<sub>2</sub> can be proposed as shown in Fig. 5g. MoO<sub>3</sub> and KCl start to form MOB at 510 °C. A saturated homogeneous solution (mixed by the MOB and MoO<sub>3</sub>) is formed after holding at 900 °C for thirty minutes, after which the highly crystalline 2D MoO<sub>2</sub> precipitates from the supersaturated solution at the cooling rate at ~ 5 °C·min<sup>−1</sup>. Without the addition of flux, MoO<sub>3</sub>

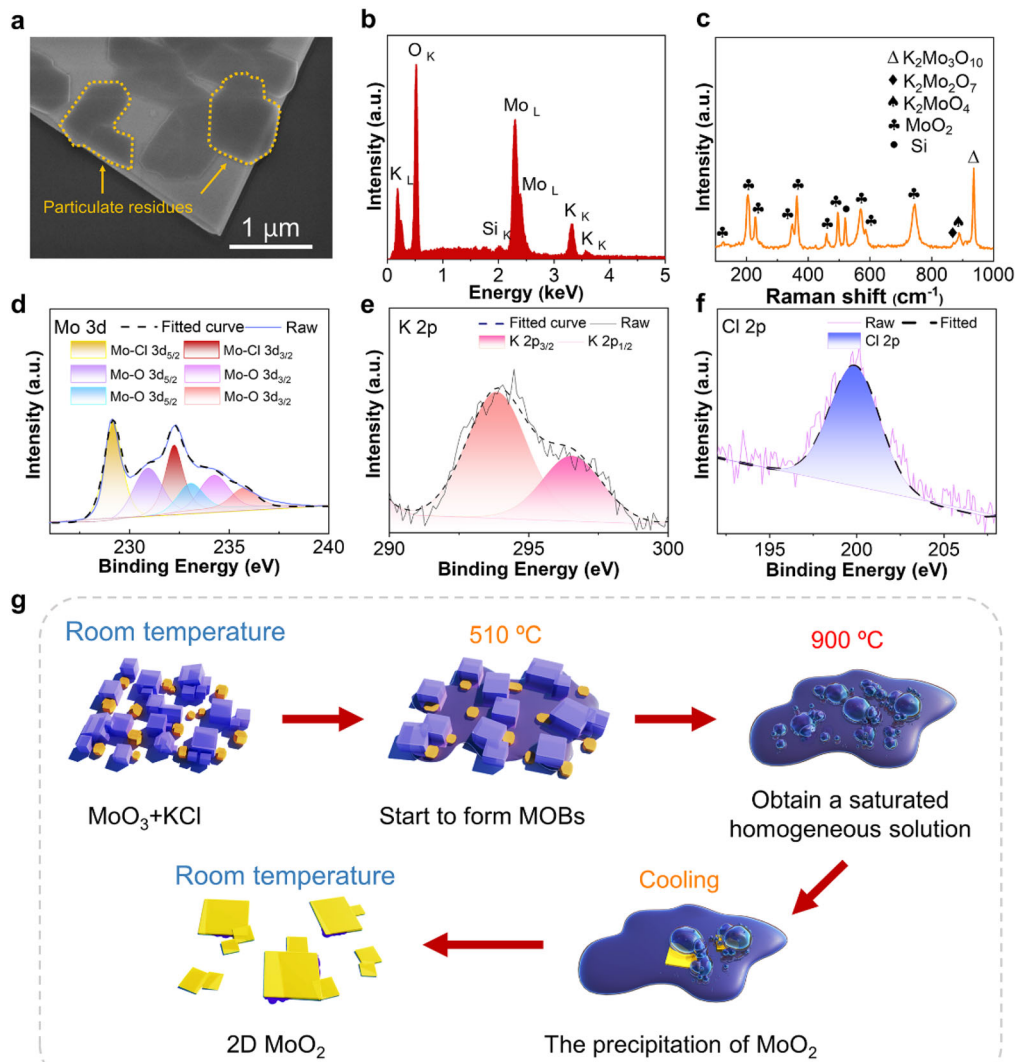
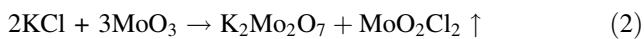
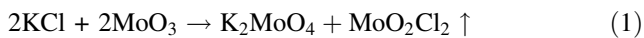


**Fig. 5** Mechanism of 2D MoO<sub>2</sub> obtained by flux method: **a** typical enlarged SEM images of flux-grown MoO<sub>2</sub> after holding at 900 °C for 30 min and cooled to room temperature at 5 °C·min<sup>-1</sup>; corresponding **b** EDS and **c** Raman spectra; XPS spectra of **d** Mo 3d, **e** K 2p and **f** Cl 2p of sample; **g** schematic illustration of 2D MoO<sub>2</sub> obtained by flux method

powder yields MoO<sub>3</sub> flakes at ~ 700 °C, followed by 3D MoO<sub>2</sub> formation at ~ 900 °C.

The possible reaction routes we propose are as follows [39, 57–59]:



Finally, the 2D MoO<sub>2</sub> is precipitated from a supersaturated solution, which contains K<sub>2</sub>Mo<sub>2</sub>O<sub>7</sub>, K<sub>2</sub>Mo<sub>3</sub>O<sub>10</sub> and K<sub>2</sub>MoO<sub>4</sub> and MoO<sub>3</sub>.

### 3.3 Electrical properties of 2D MoO<sub>2</sub>

To evaluate the electrical performance of the materials, we calculated the density of states (DOS) of the bulk and 2D

MoO<sub>2</sub> films with O-terminated (100) surfaces. It is found that the MoO<sub>2</sub> crystal is metallic and the DOS has a low valley at the Fermi level (Fig. 6a, d), which is similar to the previous calculations [56, 60]. The DOS of two layers and four layers O-terminated MoO<sub>2</sub> (100) surfaces is very close to that of MoO<sub>2</sub> crystal, both being metallic with DOSs near the Fermi level (Fig. 6b, c, e, f). Figure 6e, f exhibits relatively large peaks in DOS at  $E_F$ , suggesting electronic instability, which may be beneficial for electron transport. The experimental results show that there is no shift in the in-plane current ( $I$ )-voltage ( $V$ ) dependence when the gate voltage is modulated from -40 to 40 V as shown in Figure S11. Figure 6g depicts the  $I$ - $V$  dependence of the MoO<sub>2</sub> device. The insets are the schematic illustration and OM image of a typical device made in this work. We measured the sheet resistance of several devices and plotted them as histograms as shown in Fig. 6h, where the

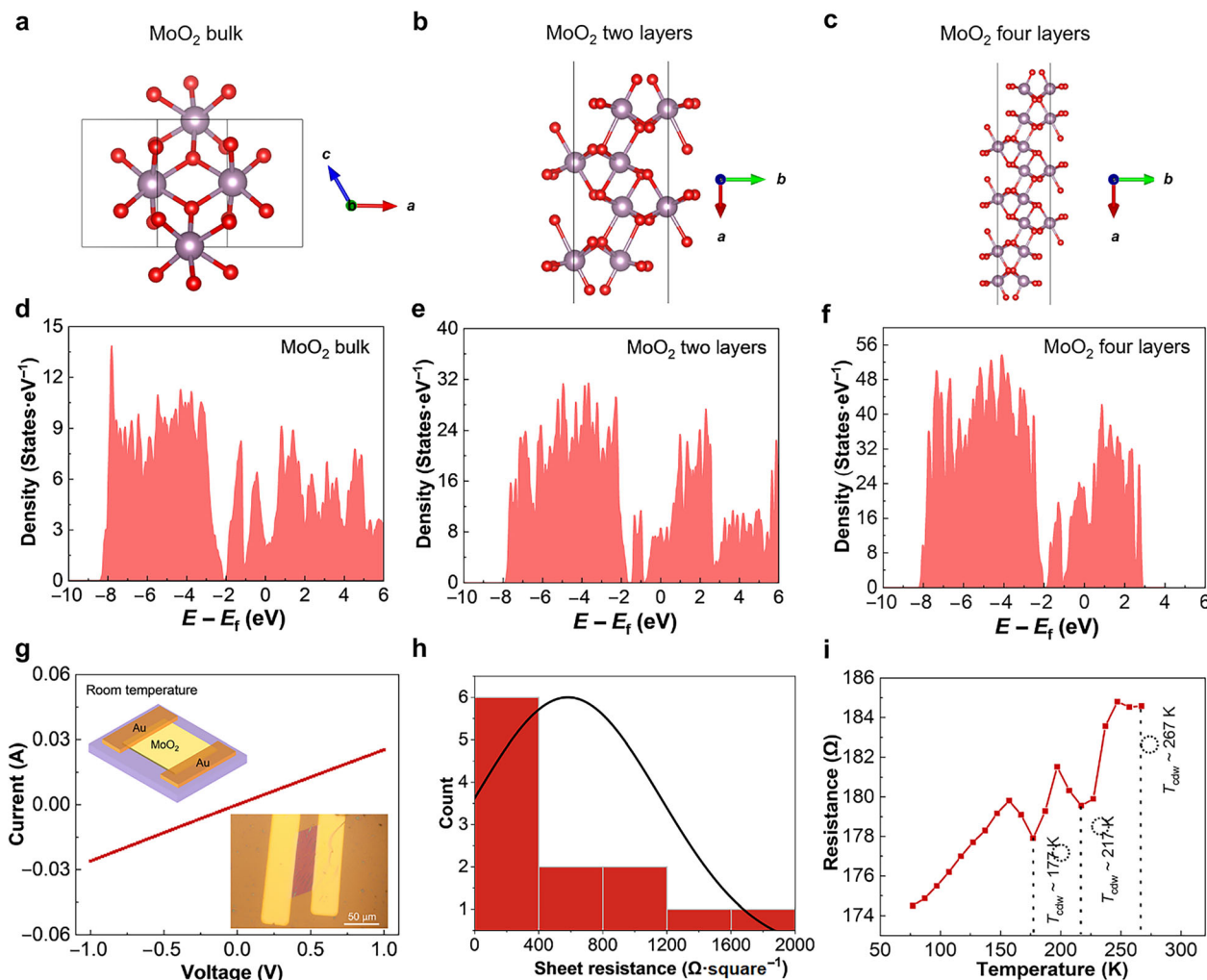


**Fig. 6** Electrical properties of 2D MoO<sub>2</sub>: structure of **a** MoO<sub>2</sub> bulk crystal, **b** two layers and **c** four layers of O-terminated MoO<sub>2</sub> (100) flakes; DOSs of **d** bulk MoO<sub>2</sub> crystal, **e** two layers thick MoO<sub>2</sub> flake and **f** four layers thick MoO<sub>2</sub> flake with O-terminated (100) surfaces; **g**  $I$ - $V$  dependence for MoO<sub>2</sub> device at room temperature and (insets) schematic illustration and OM image of flux-grown MoO<sub>2</sub> device; **h** histogram of measured sheet resistance distribution of flux-grown MoO<sub>2</sub> devices; **i** resistance vs. temperature of flux-grown MoO<sub>2</sub> devices

value could be as low as  $99 \Omega\text{-square}^{-1}$ , indicating the good conductivity of 2D MoO<sub>2</sub>, which may be ascribed to the high crystallinity that turns into less scattering. To further determine the temperature-dependent electrical properties, the resistivity was measured as a function of temperature. In Fig. 6i, kinks are observed at  $\sim 177$ ,  $217$  and  $267$  K. The exact origin of the kinks is still under investigation. However, it is reasonable to attribute them to the metal-semiconductor transition caused by the so-called charge density wave (CDW) instabilities. CDW is a periodic modulation of electron density, which is accompanied by periodic lattice distortions and is mostly observed in low-dimensional materials [61–65]. In fact, as early as the 1960s, the behavior has been demonstrated experimentally in a variety of quasi-low-dimensional compounds, such as MOBs [61]. For example, the blue bronzes ( $\text{K}_{0.3}\text{MoO}_3$ ),

which is one of the MOBs, are metallic at ambient temperatures but exhibit a metal-to-semiconductor transition at  $T_P = 180$  K [66]. The layered purple bronze  $\text{K}_{0.9}\text{Mo}_6\text{O}_{17}$  has a triple-Q CDW phase below  $T_c = \sim 120$  K [67]. Furthermore, it has been reported that doping MoO<sub>2</sub> with  $\text{K}^+$  can induce superconductivity and anomalous metallic conductivity [68], where two phase transitions have been observed in the compound, one at  $\sim 54$  K and another near room temperature. An explanation as to why the CDW phase transition arises in certain low-dimensional materials has been provided by Pouget et al. [69]. Typically, in an energy band of a 2D metal, when the Fermi surfaces in  $k$ -space are two parallel lines, one line can be superposed to the other line by a translational vector. In this case, the Fermi surface is said to be nested by the vector. Here, the occupied and unoccupied band levels (near the Fermi



surface) related by the nesting vector are roughly degenerate. Nevertheless, under a certain perturbation, a small energy gap at the Fermi level can be introduced by virtue of CDW caused by the interaction between those band levels [69]. For a realistic 2D metal with several partially overlapping energy bands, even if the Fermi surface nesting does not exist at a first glance, “hidden nesting” may still happen as long as the band structures fulfill certain requirements, which could anyway lead to CDW related metal-to-semiconductor transition [69]. Detailed discussion is out of the scope of this paper. We note that in electrical measurement, it may be reflected by kinks in resistance–temperature curves where metal-to-semiconductor phase transitions occur, such as the phenomenon observed in Fig. 6i. The three kinks appearing in Fig. 6i may be due to different CDW phase transitions happening at different temperatures.

## 4 Conclusion

In conclusion, we have showcased the efficacy of flux growth in synthesizing 2D MoO<sub>2</sub> flakes via CVD. This method presents notable benefits in achieving reduced thickness and expanded dimensions when contrasted with traditional approaches. Additionally, the resulting 2D MoO<sub>2</sub> shows high crystallinity and good conductivity and exhibits the CDW phenomenon in the measurement of resistivity as a function of temperatures. We demonstrate that the prevailing MSAM in the 2D community is in fact the flux method. We have conducted a systematic investigation into the impact of temperature, homogeneous time and cooling rate on growth products. This aims to extend the application of the flux method, commonly employed for synthesizing bulk single crystals, to non-layered 2DMOs and complete the understanding of the MSAM for the preparation of non-layered materials. We anticipate that by further refinement, thinner and larger areas of 2D non-layered materials prepared by the flux method can be achieved, with the possibility of extending to layered materials, assisting in the further exploration of their properties and applications.

**Acknowledgements** The study was financially supported by the National Key Research and Development Program of China (Nos. 2023YFB3608703 and 2023YFB3608700), Fujian Science & Technology Innovation Laboratory for Optoelectronic Information of China (Nos. 2021ZZ122 and 2020ZZ110) and Fujian provincial projects (Nos. 2021HZ0114 and 2021J01583).

**Funding** Open access funding provided by Chalmers University of Technology.

## Declarations

**Conflict of interest** The authors declare that they have no conflict of interest

**Open Access** This article is licensed under a Creative Commons Attribution 4.0 International License, which permits use, sharing, adaptation, distribution and reproduction in any medium or format, as long as you give appropriate credit to the original author(s) and the source, provide a link to the Creative Commons licence, and indicate if changes were made. The images or other third party material in this article are included in the article's Creative Commons licence, unless indicated otherwise in a credit line to the material. If material is not included in the article's Creative Commons licence and your intended use is not permitted by statutory regulation or exceeds the permitted use, you will need to obtain permission directly from the copyright holder. To view a copy of this licence, visit <http://creativecommons.org/licenses/by/4.0/>.

## References

- [1] Wang JH, Yang SW, Ma FB, Zhao YK, Zhao SN, Xiong ZY, Cai D, Shen HD, Zhu K, Zhang QY, Cao YL, Wang TS, Zhang HP. RuCo alloy nanoparticles embedded within N-doped porous two-dimensional carbon nanosheets: a high-performance hydrogen evolution reaction catalyst. *Tungsten*. 2024;6(1):114. <https://doi.org/10.1007/s42864-023-00223-3>.
- [2] Wang XL, Chen YZ, Chang ZH, Lin YC, Ma JY. A homopolymolybdate-supported plate-like 2D cobalt network constructed from a new pyrazole-amide-pyridyl ligand: highly electrochemical activity in both capacitive performance and the detection of Cr (VI). *Tungsten*. 2024;6(2):422. <https://doi.org/10.1007/s42864-023-00220-6>.
- [3] Lan HH, Wang LY, He RZ, Huang SY, Yu JQ, Guo JM, Luo JR, Li YL, Zhang JY, Liu JX, Zhang SP, Zeng MQ, Fu L. 2D quasi-layered material with domino structure. *Nat Commun*. 2023;14(1):7225. <https://doi.org/10.1038/s41467-023-42818-x>.
- [4] Wang F, Wang Z, Shifa TA, Wen Y, Wang FM, Zhan XY, Wang QS, Xu K, Huang Y, Yin L. Two-dimensional non-layered materials: synthesis, properties and applications. *Adv Func Mater*. 2017;27(19):1603254. <https://doi.org/10.1002/adfm.201603254>.
- [5] Zheng ZQ, Yao JD, Li JB, Yang GW. Non-layered 2D materials toward advanced photoelectric devices: progress and prospects. *Mater Horiz*. 2020;7(9):2185. <https://doi.org/10.1039/D0MH00599A>.
- [6] Zhou N, Yang R, Zhai T. Two-dimensional non-layered materials. *Mater Today Nan*. 2019;8:100051. <https://doi.org/10.1016/j.mtnano.2019.100051>.
- [7] Lyu CG, Zhang LH, Zhang X, Zhang HM, Xie HG, Zhang JH, Liu YF, Liu Y, Wu RX, Zhang JR. Controlled synthesis of sub-millimeter nonlayered WO<sub>2</sub> nanoplates via a WSe<sub>2</sub>-assisted method. *Adv Mater*. 2023;35(12):2207895. <https://doi.org/10.1002/adma.202207895>.
- [8] Feng XY, Xin D, Zhang ZS, Liu JJ, Ning TY, Yu JY, Zhou WJ, Liu J. Comprehensive study on the nonlinear optical response of MoO<sub>2</sub> nanosheets in pulsed lasers. *Opt Laser Technol*. 2023; 157:108632. <https://doi.org/10.1016/j.optlastec.2022.108632>.
- [9] Zavabeti A, Ou JZ, Carey BJ, Syed N, Rebecca O-T, Mayes Edwin LH, Xu CL, Omid K, O'Mullane Anthony P, Kaner RB. A liquid metal reaction environment for the room-temperature synthesis of atomically thin metal oxides. *Science*. 2017; 358(6361):332. <https://doi.org/10.1126/science.aao4249>.
- [10] Singh K, Maurya KK, Malviya M. Review of electrochemical sensors and biosensors based on first-row transition metals



- review of electrochemical. *J Anal Test*. 2023. <https://doi.org/10.1007/s41664-023-00292-w>.
- [11] Gai LY, Lai RP, Dong XH, Wu X, Luan QT, Wang J, Lin HF, Ding WH, Wu GL, Xie WF. Recent advances in ethanol gas sensors based on metal oxide semiconductor heterojunctions. *Rare Met*. 2022;41(6):1818. <https://doi.org/10.1007/s12598-021-01937-4>.
  - [12] Lu XC, Lu YZ, Wang C, Cao Y. Efficient photoelectrodes based on two-dimensional transition metal dichalcogenides heterostructures: from design to construction. *Rare Met*. 2022; 41(4):1142. <https://doi.org/10.1007/s12598-021-01875-1>.
  - [13] Jiang HL, Pan J, Zhou W, Li HM, Liu S. Fabrication and application of arrays related to two-dimensional materials. *Rare Met*. 2022;41(1):262. <https://doi.org/10.1007/s12598-021-01842-w>.
  - [14] Zhang HM, Wu YW, Huang ZW, Shen XH, Li BL, Zhang ZC, Wu RX, Wang D, Yi C, He K. Synthesis of two-dimensional MoO<sub>2</sub> nanoplates with large linear magnetoresistance and non-linear hall effect. *Nano Lett*. 2023;23(6):2179. <https://doi.org/10.1021/acs.nanolett.2c04721>.
  - [15] Apte A, Mozaffari K, Samghabadi FS, Hachtel JA, Chang L, Susarla S, Idrobo JC, Moore DC, Glavin NR, Litvinov D. 2D electrets of ultrathin MoO<sub>2</sub> with apparent piezoelectricity. *Adv Mater*. 2020;32(24):2000006. <https://doi.org/10.1002/adma.202000006>.
  - [16] Wazir N, Liu RB, Ding CJ, Wang XS, Ye X, Lingling X, Lu TQ, Wei L, Zou BS. Vertically stacked MoSe<sub>2</sub>/MoO<sub>2</sub> nanolayered photodetectors with tunable photoresponses. *ACS Appl Nano Mater*. 2020;3(8):7543. <https://doi.org/10.1021/acsanm.0c01195>.
  - [17] Luo JJ, Chen HX, Wang J, Xia FF, Huang XT. Direct growth of 2D MoO<sub>2</sub> single crystal on SiO<sub>2</sub>/Si substrate by atmospheric pressure chemical vapor deposition. *Mater Chem Phys*. 2020; 251:123166. <https://doi.org/10.1016/j.matchemphys.2020.123166>.
  - [18] Wu QK, Luo YT, Xie RK, Nong HY, Cai ZY, Tang L, Tan JY, Feng SM, Zhao SL, Yu QM. Space-confined one-step growth of 2D MoO<sub>2</sub>/MoS<sub>2</sub> vertical heterostructures for superior hydrogen evolution in alkaline electrolytes. *Small*. 2022;18(32):2201051. <https://doi.org/10.1002/smll.202201051>.
  - [19] Fang LZ, Liu HW, Guan W, Zheng BY, Liang JY, Wang TH, Zhu XL, Li SY, Li D, Pan AL. Controlled synthesis of ultrathin metallic MoO<sub>2</sub> nanosheets for van der Waals contact. *Sci China Mater*. 2022. <https://doi.org/10.1007/s40843-022-2260-6>.
  - [20] Pu EQ, Liu DB, Ren PY, Zhou WC, Tang DS, Xiang BC, Wang YH, Miao JS. Ultrathin MoO<sub>2</sub> nanosheets with good thermal stability and high conductivity. *AIP Adv*. 2017;7(2):025015. <https://doi.org/10.1063/1.4977543>.
  - [21] Vorobeva NS, Lipatov A, Muratov DS, Sinitskii A. Chemical vapor deposition and characterization of two-dimensional molybdenum dioxide (MoO<sub>2</sub>) nanoplatelets. *Nanotechnology*. 2018;29(50):505707. <https://doi.org/10.1088/1361-6528/aae366>.
  - [22] Deng LY, Li WY, Sun J, Wang XH, Zhang Q, Lin C, Pan K, Yan Q, Cheng SY. Can fluorophlogopite mica be used as an alkali metal ion source to boost the growth of two-dimensional molybdenum dioxide? *Appl Surf Sci*. 2023;612:155853. <https://doi.org/10.1016/j.apsusc.2022.155853>.
  - [23] Jacco JC, Loiacono GM, Jaso M, Mizell G, Greenberg B. Flux growth and properties of KTiOPO<sub>4</sub>. *J Cryst Growth*. 1984; 70(1–2):484. [https://doi.org/10.1016/0022-0248\(84\)90306-3](https://doi.org/10.1016/0022-0248(84)90306-3).
  - [24] Tachibana M. 2017 Beginner's Guide to Flux Crystal Growth. In: Naoki OHASHI, Takahito O, Yoshitaka T, Takashi T, Kazuya T, Masanobu N, Nobutaka H, Kenjiro M.(Eds.). Tokyo, Springer; 2017.
  - [25] Bugaris DE, Zur LHC. Materials discovery by flux crystal growth: quaternary and higher order oxides. *Angew Chem Int Ed*. 2012;51(16):3780. <https://doi.org/10.1002/anie.201102676>.
  - [26] May AF, Yan JQ, McGuire MA. A practical guide for crystal growth of van der Waals layered materials. *J Appl Phys*. 2020; 128(5):051101. <https://doi.org/10.1063/5.0015971>.
  - [27] Elwell D. Fundamentals of flux growth. Arend H, Hulliger J, editors. In: *Crystal Growth in Science and Technology*. Boston: Springer; 1989. 133.
  - [28] Kuznetsov AB, Kokh KA, Kononova NG, Shevchenko VS, Kaneva EV, Uralbekov B, Svetlichnyi VA, Kokh AE. Synthesis and growth of new rare earth borates KCaR(BO<sub>3</sub>)<sub>2</sub> (R= La, Pr and Nd). *J Solid State Chem*. 2020;282:121091. <https://doi.org/10.1016/j.jssc.2019.121091>.
  - [29] Hoffman TB, Clubine B, Zhang Y, Snow K, Edgar JH. Optimization of Ni–Cr flux growth for hexagonal boron nitride single crystals. *J Cryst Growth*. 2014;393:114. <https://doi.org/10.1016/j.jcrysgro.2013.09.030>.
  - [30] Wanklyn BM. Flux growth of some complex oxide materials. *J Mater Sci*. 1972;7(7):813. <https://doi.org/10.1007/BF00549910>.
  - [31] Li XS, Cai WW, An JH, Kim SY, Nah JH, Yang DX, Piner R, Velamakanni A, Jung I, Tutuc E. Large-area synthesis of high-quality and uniform graphene films on copper foils. *Science*. 2009;324(5932):1312. <https://doi.org/10.1126/science.1171245>.
  - [32] Park JH, Park JC, Yun SJ, Kim H, Luong DH, Kim SM, Choi SH, Yang W, Kong J, Kim KK. Large-area monolayer hexagonal boron nitride on Pt foil. *ACS Nano*. 2014;8(8):8520. <https://doi.org/10.1021/nn503140y>.
  - [33] Li XS, Cai WW, Colombo L, Ruoff RS. Evolution of graphene growth on Ni and Cu by carbon isotope labeling. *Nano Lett*. 2009;9(12):4268. <https://doi.org/10.1021/nl902515k>.
  - [34] Kim SM, Hsu A, Park MH, Chae SH, Yun SJ, Lee JS, Cho DH, Fang WJ, Lee CG, Palacios T. Synthesis of large-area multilayer hexagonal boron nitride for high material performance. *Nat Commun*. 2015;6(1):1. <https://doi.org/10.1038/ncomms7999>.
  - [35] Volkova EA, Maltsev VV, Leonyuk NI. Flux growth of NdAl<sub>3</sub>(BO<sub>3</sub>)<sub>4</sub> single crystals from a K<sub>2</sub>Mo<sub>3</sub>O<sub>10</sub> based system. *Cryst Eng Comm*. 2017;19(7):1071. <https://doi.org/10.1039/C6CE02390H>.
  - [36] Li SS, Lin YC, Zhao W, Wu J, Wang Z, Hu ZH, Shen YD, Tang DM, Wang JY, Zhang Q. Vapour–liquid–solid growth of monolayer MoS<sub>2</sub> nanoribbons. *Nat Mater*. 2018;17(6):535. <https://doi.org/10.1038/s41563-018-0055-z>.
  - [37] Chen JY, Zhao XX, Tan SJR, Xu H, Wu B, Liu B, Fu DY, Fu W, Geng DC, Liu YP. Chemical vapor deposition of large-size monolayer MoSe<sub>2</sub> crystals on molten glass. *J Am Chem Soc*. 2017;139(3):1073. <https://doi.org/10.1021/jacs.6b12156>.
  - [38] Suzuki H, Kaneko T, Shibuta Y, Ohno M, Maekawa Y, Kato T. Wafer-scale fabrication and growth dynamics of suspended graphene nanoribbon arrays. *Nat Commun*. 2016;7(1):1. <https://doi.org/10.1038/ncomms11797>.
  - [39] Zhou JD, Lin JH, Huang XW, Zhou Y, Chen Y, Xia J, Wang H, Xie Y, Yu HM, Lei JC. A library of atomically thin metal chalcogenides. *Nature*. 2018;556(7701):355. <https://doi.org/10.1038/s41586-018-0008-3>.
  - [40] Zhou K, Shang G, Hsu HH, Han ST, Roy Vellaisamy AL, Ye Z. Emerging 2D metal oxides: from synthesis to device integration. *Adv Mater*. 2023;35(21):2207774. <https://doi.org/10.1002/adma.202207774>.
  - [41] Momma K, Izumi F. VESTA 3 for three-dimensional visualization of crystal. volumetric and morphology data. *J Appl Crystallogr*. 2011;44(6):1272. <https://doi.org/10.1107/S0021889811038970>.
  - [42] Spevack PA, McIntyre NS. Thermal reduction of molybdenum trioxide. *J Phys Chem*. 1992;96(22):9029. <https://doi.org/10.1021/j100201a062>.
  - [43] Dieterle M, Weinberg G, Mestl G. Raman spectroscopy of molybdenum oxides Part I structural characterization of oxygen defects in MoO<sub>3-x</sub> by DR UV/VIS, Raman spectroscopy and



- X-ray diffraction. *Phys Chem Chem Phys*. 2002;4(5):812. <https://doi.org/10.1039/B107012F>.
- [44] Lin LH, Lin ZY, Zhang J, Cai X, Lin W, Yu ZY, Wang XC. Molecular-level insights on the reactive facet of carbon nitride single crystals photocatalysing overall water splitting. *Nat Catal*. 2020;3(8):649. <https://doi.org/10.1038/s41929-020-0476-3>.
- [45] Scheel HJ, Elwell D. Stable growth rates and temperature programming in flux growth. *J Cryst Growth*. 1972;12(2):153. [https://doi.org/10.1016/0022-0248\(72\)90045-0](https://doi.org/10.1016/0022-0248(72)90045-0).
- [46] Arreola VMA, Salazar MF, Zhang TY, Wang K, Aguilar AHB, Reddy KCS, Strupiechonski E, Terrones M, Bugallo AD. Direct growth of monolayer 1T-2H MoS<sub>2</sub> heterostructures using KCl-assisted CVD process. *2D Materials*. 2021;8(2):025033. <https://doi.org/10.1088/2053-1583/abe739>.
- [47] Han W, Liu KL, Yang SJ, Wang FK, Su JW, Jin B, Li HQ, Zhai TY. Salt-assisted chemical vapor deposition of two-dimensional materials. *Science China Chem*. 2019;62(10):1300. <https://doi.org/10.1007/s11426-019-9525-y>.
- [48] Wang M, You JL, Sobol AA, Wang J, Wu J, Lv XM. Temperature-dependent Raman spectroscopic studies of microstructure present in dipotassium molybdate crystals and their melts. *J Raman Spectrosc*. 2016;47(10):1259. <https://doi.org/10.1002/jrs.4948>.
- [49] Balendhran S, Deng JK, Ou JZ, Walia S, Scott J, Tang JS, Wang KL, Field Matthew R, Salvy R, Serge Z. Enhanced charge carrier mobility in two-dimensional high dielectric molybdenum oxide. *Adv Mater*. 2013;25(1):109. <https://doi.org/10.1002/adma.201203346>.
- [50] Seguin L, Figlarz M, Cavagnat R, Lassègues J-C. Infrared and Raman spectra of MoO<sub>3</sub> molybdenum trioxides and MoO<sub>3</sub>·xH<sub>2</sub>O molybdenum trioxide hydrates. *Spectrochim Acta Part A Mol Biomol Spectrosc*. 1995;51(8):1323. [https://doi.org/10.1016/0584-8539\(94\)00247-9](https://doi.org/10.1016/0584-8539(94)00247-9).
- [51] Zheng BJ, Wang ZG, Chen YF, Zhang WL, Li XS. Centimeter-sized 2D  $\alpha$ -MoO<sub>3</sub> single crystal: growth, Raman anisotropy, and optoelectronic properties. *2D Materials*. 2018;5(4):045011. <https://doi.org/10.1088/2053-1583/aad2ba>.
- [52] Dieterle M, Mestl G. Raman spectroscopy of molybdenum oxides Part II Resonance Raman spectroscopic characterization of the molybdenum oxides Mo<sub>4</sub>O<sub>11</sub> and MoO<sub>2</sub>. *Phys Chem Chem Phys*. 2002;4(5):822.
- [53] Chen CK. Relationship between crystal growth, structure and spectral characteristics of NdAl<sub>3</sub>(BO<sub>3</sub>)<sub>4</sub> with order-disorder structure. *J Cryst Growth*. 1988;89(2-3):295. [https://doi.org/10.1016/0022-0248\(88\)90413-7](https://doi.org/10.1016/0022-0248(88)90413-7).
- [54] Karlsson S, Pettersson J, Johansson LG, Svensson J-E. Alkali induced high temperature corrosion of stainless steel: the influence of NaCl, KCl and CaCl<sub>2</sub>. *Oxid Met*. 2012;78:83. <https://doi.org/10.1007/s11085-012-9293-7>.
- [55] Wu HM, Chen SA. Dopant-polymer interaction: MoCl<sub>5</sub>-doped polyacetylene. *Synth Met*. 1988;26(3):225. [https://doi.org/10.1016/0379-6779\(88\)90239-1](https://doi.org/10.1016/0379-6779(88)90239-1).
- [56] Haycock D, Urch DS, Garner CD, Hillier IH. Electronic structure of the octachlorodimolybdenum (II) anion using X-ray emission and X-ray photoelectron spectroscopies. *J Electron Spectrosc Relat Phenom*. 1979;17(5):345. [https://doi.org/10.1016/0368-2048\(79\)80009-2](https://doi.org/10.1016/0368-2048(79)80009-2).
- [57] Wang P, Lei JY, Qu JF, Cao SY, Jiang H, He MC, Shi HY, Sun XD, Gao B, Liu WJ. Mechanism of alkali metal compound-promoted growth of monolayer MoS<sub>2</sub>: eutectic intermediates. *Chem Mater*. 2019;31(3):873. <https://doi.org/10.1021/acs.chemmater.8b04022>.
- [58] Pilipenko OV, Mal'tsev VV, Koporulina EV, Leonyuk NI, Tolstik NA, Kuleshov NV. Growth of (Er, Yb): YAl<sub>3</sub>(BO<sub>3</sub>)<sub>4</sub> laser crystals. *Crystallogr Rep*. 2008;53:336. <https://doi.org/10.1134/S1063774508020260>.
- [59] Wold A, Kunmann W, Arnott RJ, Ferretti A. Preparation and properties of sodium and potassium molybdenum bronze crystals. *Inorg Chem*. 1964;3(4):545. <https://doi.org/10.1021/ic50014a022>.
- [60] Parker D, Idrobo JC, Cantoni C, Sefat AS. Evidence for superconductivity at T<sub>c</sub> = 12 K in oxygen-deficient MoO<sub>2- $\delta$</sub>  and properties of molybdenum arsenide and oxide binaries. *Phys Rev B*. 2014;90(5):054505. <https://doi.org/10.1103/PhysRevB.90.054505>.
- [61] Greenblatt M. Molybdenum oxide bronzes with quasi-low-dimensional properties. *Chem Rev*. 1988;88(1):31. <https://doi.org/10.1021/cr00083a002>.
- [62] Banks E, Wold A. Preparative Inorganic Reactions. In: Jolly WL, editor. *Evjhg*. New York: Wiley; 1968.
- [63] Beille J, Rötger A, Dumas J, Schlenker C. Effect of hydrostatic pressure on the resistivity of the charge-density-wave compound KMo<sub>6</sub>O<sub>17</sub>. *Philos Mag Lett*. 1991;64(4):221. <https://doi.org/10.1080/09500839108214546>.
- [64] Hulliger F. Physics and chemistry of materials with layered structures. Lévy FA, editor. In: *Crystallography and crystal Chemistry of Materials with Layered Structure*. UK: Springer; 1976.
- [65] Toombs GA. Quasi-one-dimensional conductors. *Phys Rep*. 1978;40(3):181. [https://doi.org/10.1016/0370-1573\(78\)90149-7](https://doi.org/10.1016/0370-1573(78)90149-7).
- [66] Nikiforov MP, Isakovic Abdel F, Bonnell DA. Atomic structure and charge-density waves of blue bronze K<sub>0.3</sub>MoO<sub>3</sub> (201) by variable-temperature scanning tunneling microscopy. *Phys Rev B*. 2007;76(3):033104. <https://doi.org/10.1103/PhysRevB.76.033104>.
- [67] Su L, Hsu CH, Lin H, Pereira VM. Charge density waves and the hidden nesting of purple bronze K<sub>0.9</sub>Mo<sub>6</sub>O<sub>17</sub>. *Phys Rev Lett*. 2017;118(25):257601. <https://doi.org/10.1103/PhysRevLett.118.257601>.
- [68] Alves LMS, de Lima BS, dos Santos CAM, Rebello A, Masunaga SH, Neumeier JJ, Leao JB. Phase transitions in K-doped MoO<sub>2</sub>. *J Appl Phys*. 2014;115(20):204912. <https://doi.org/10.1063/1.4879096>.
- [69] Whangbo MH, Canadell E, Foury P, Pouget JP. Hidden Fermi surface nesting and charge density wave instability in low-dimensional metals. *Science*. 1991;252(5002):96. <https://doi.org/10.1126/science.252.5002.96>.